RSC Advances

PAPER

View Article Online
View Journal | View Issue

Cite this: *RSC Adv.*, 2026, **16**, 6900

Strain effect on photocatalytic oxygen evolution activity in Sr_3NF_3 mixed anion perovskite using first-principles density functional theory (DFT)

Parmith Utsho,[a] Manik Ibrahim,[b] Md. Sakib Hasan Khan *[a] and Md. Rafiqul Islam[a]

This work presents a first-principles investigation of the mixed-anion perovskite Sr_3NF_3, evaluating its photocatalytic potential under biaxial strain. Stability analysis confirms its structural, dynamic and mechanical robustness. Sr_3NF_3 exhibits a direct bandgap of 2.06 eV (HSE06), tunable from 1.77 eV under +6% tensile strain to 2.16 eV under −6% compressive strain. Electron density difference plots reveal strong internal charge separation attributed to the mixed-anion framework. Optical results show that Sr_3NF_3 exhibits high absorption in both visible and UV regions, with compressive strain enhancing absorption ($\sim 1.35 \times 10^5$ cm^{-1}) and the static dielectric constant ($\varepsilon = 4.11$), improving carrier separation. While unsuitable for hydrogen evolution, Sr_3NF_3 shows strong intrinsic oxidation driving force for oxygen evolution, exhibiting an overpotential of 1.51 eV at −6% strain. Low carrier effective masses further suggest fast charge transport. These findings identify Sr_3NF_3 as a promising, strain-tunable mixed-anion perovskite with favorable intrinsic electronic properties for oxygen evolution, and suitable as an OER-oriented component in advanced photocatalytic architectures.

Received 10th November 2025
Accepted 27th January 2026

DOI: 10.1039/d5ra08652c

rsc.li/rsc-advances

1. Introduction

The growing energy demands of the world and the pressing need to reduce CO_2 emissions have led to elevated efforts towards finding sustainable and carbon-free energy alternatives.[1] Hydrogen (H_2) stands out as a potential fuel choice in this issue because its combustion emits only water (H_2O), making it a green alternative with a high energy density.[2] However, traditional approaches of producing H_2, like coal gasification and steam methane reforming (SMR), are both costly and energy-intensive and produce 9–26 kg CO_2 per kilogram of H_2 produced.[3] Photocatalytic water splitting (PWS) provides a more environmentally friendly, more cost-effective process of hydrogen production by using sunlight to excite electrons and holes in a semiconductor catalyst.[4] The electrons and holes then move to the surrounding pure water. Subsequently, the electrons (holes) drive the hydrogen (oxygen) evolution reaction to produce H_2 (O_2) from water.[5]

For effective photocatalysis, the material must exhibit proper electronic properties: its bandgap must exceed 1.23 eV,[6] the conduction band edge (CBE) must lie above H^+/H_2 redox level for reduction (−4.03 eV with respect to vacuum) and valence band edge (VBE) should lie below O_2/H_2O redox level for oxidation (−5.26 eV with respect to vacuum).[7] For overall water splitting to occur, both half-reactions are necessary, but the oxygen evolution reaction (OER) presents a greater challenge because of its four-electron reaction pathway, acting as the principal kinetic bottleneck in the process.[8] Therefore, developing efficient OER catalysts is critical for improving the overall efficiency of PWS systems.[9]

Among various semiconductor families investigated for photocatalysis, perovskite-structured materials became especially promising options because of their structural versatility, tunable electronic properties and inherent stability.[10] A major breakthrough in perovskite photocatalyst research came with the introduction of mixed-anion compounds. The incorporation of nitrogen or mixed halide species into perovskite structures reduces the bandgap compared to conventional oxide perovskites, making them particularly attractive as visible-light-driven photocatalysts.[11] The solid solution of gallium nitride and zinc oxide ($Ga_{1-x}Zn_x$) ($N_{1-x}O_x$) represents a historical landmark as one of the first non-oxide systems to achieve overall water splitting under visible light.[12] However, its absorption edge is typically limited to <500 nm, restricting its maximum theoretical efficiency. Materials like $BaTaO_2N$ ($E_g \sim$ 1.9 eV) and $SrTaO_2N$ ($E_g \sim 2.1$ eV) are capable of absorbing light up to 600–660 nm.[13,14] They have demonstrated activity for both hydrogen and oxygen evolution in the presence of sacrificial reagents. Despite this, the synthesis of defect-free oxynitrides remains highly challenging and their performance is often limited by rapid charge-carrier recombination.[15] More complex

[a]*Department of Electrical and Electronic Engineering, Khulna University of Engineering & Technology, Khulna-9203, Bangladesh. E-mail: sakib@eee.kuet.ac.bd*
[b]*Department of Energy Science and Engineering, Khulna University of Engineering & Technology, Khulna-9203, Bangladesh*

quaternary systems such as $LaMg_{1/3}Ta_{2/3}O_2N$ have further demonstrated one-step overall water splitting under visible-light irradiation up to 600 nm; however, they suffer from sluggish surface reaction kinetics.[16] Oxysulfides like $Y_2Ti_2O_5S_2$ exhibit efficient charge separation but contain extremely unstable sulfide ions (S^{2-}), leading to rapid material degradation.[17] In contrast, oxyhalides like Bi_4NbO_8Cl demonstrated highly stable oxygen evolution without the rapid degradation. But it has wider bandgap ($E_g \sim 2.4$ eV) compared to the narrowest oxynitrides, limiting absorption to the blue/green region of the spectrum.[18] Beyond oxynitrides, oxysulfides and oxyhalides mixed-anion perovskites with more complex anion chemistries remain largely unexplored for photocatalytic applications. Among them, the A_3BX_3 family of perovskites, where A denotes alkaline earth cation, B denotes pnictide anion and X denotes halide, have emerged as attractive solar-water splitting materials. Unlike traditional mixed-anion perovskites consisting of group VI–V anions, the A_3BX_3 framework introduces a unique group-V/halogen interaction. This interaction may enable strain-induced modulation of orbital hybridization and valence-band chemistry, offering new insight into bandgap tuning and photocatalytic activity. Moreover, the differing electronegativity between B^{3-} and X^- induces internal charge polarization, which enhances charge separation and suppresses electron–hole recombination. These materials can also show optical and electronic characteristics comparable to conventional halide perovskites such as adequate bandgaps and excellent thermal stability.[19] Despite these advantages, the photocatalytic potential of A_3BX_3 perovskites has received little attention to date.

Sr_3NF_3 belongs to the family of A_3BX_3 perovskites consisting of strontium (Sr^{2+}), nitride (N^{3-}) and fluoride (F^-) ions. The nitride anions lead to an elevated valence band because they have higher-energy 2p orbitals compared to halides or oxides, thereby increasing the absorption of visible light and facilitating the OER.[20] On the other hand, since fluoride ions have high electronegativity, they increase the structural stability and can lead to a moderate band gap that can be useful in solar light harvesting.[21] The Sr^{2+} cations contribute spatially extended 5s/4d orbitals to the conduction band, which broaden the conduction band and can support more delocalized electronic states, favouring higher carrier mobility. Additionally, the all-inorganic composition suggests superior thermal and chemical stability under operating conditions. Due to these compositional and structural characteristics, Sr_3NF_3 can have promising photocatalytic activity. The photocatalytic performance of Sr_3NF_3 can be further improved by employing strain engineering, which allows fine-tuning of key material properties, such as bandgap, band edge alignment, carrier effective masses and optical absorption characteristics, without altering the chemical composition.[22] Despite this potential, the intrinsic and strain-dependent photocatalytic properties of Sr_3NF_3 have not yet been systematically explored. In this study, we therefore use first-principles calculation to investigate how biaxial strain influences its fundamental characteristics and photocatalytic potential. Our results reveal that while pristine Sr_3NF_3 is thermodynamically unfavourable for hydrogen evolution, biaxial strain significantly improves its valence-band oxidation power and optical absorption, identifying it as a tunable OER photocatalyst candidate.

2. Computational methodology

All first-principles calculations were conducted using the Cambridge Serial Total Energy Package (CASTEP) code, which operates within the density functional theory (DFT) framework.[23,24] The atomic structure of Sr_3NF_3 was visualized by the VESTA software.[25] The crystal structure was geometry optimized using the Broyden–Fletcher–Goldfarb–Shanno (BFGS) minimization algorithm with a norm-conserving pseudopotential.[26] A plane-wave energy cutoff of 980 eV was employed during structural relaxation to eliminate basis-set incompleteness errors. To ensure numerical reliability, a convergence test of the total energy with respect to the *k*-point mesh was performed using the GGA-PBE functional, varying the Monkhorst–Pack grid from $1 \times 1 \times 1$ to $10 \times 10 \times 10$, as shown in Fig. S1 (SI). The total energy converges and reaches its minimum at a $2 \times 2 \times 2$ *k*-point grid, with negligible changes upon further increasing the mesh density. Accordingly, a $2 \times 2 \times 2$ *k*-point mesh was adopted for geometry optimization and elastic constant calculations to ensure computational efficiency while maintaining accuracy. The convergence thresholds for energy, maximum stress, maximum displacement and maximum force was 5×10^{-6} eV per atom, 0.02 GPa, 5×10^{-4} Å and 0.01 eV $Å^{-1}$, respectively. The electronic band structure was initially calculated using the Generalized Gradient Approximation (GGA), specifically the Perdew–Burke–Ernzerhof (PBE) functional. To compensate for the common underestimation of the bandgap by GGA-PBE, we later employed the more accurate Heyd–Scuseria–Ernzerhof (HSE06) hybrid functional.[27] Because electronic and optical properties are more sensitive to Brillouin-zone sampling, denser *k*-point meshes were used for these calculations. Specifically, a $4 \times 4 \times 4$ *k*-point grid was used for band structure calculations, an $8 \times 8 \times 8$ grid for density of states (DOS and PDOS), and a $12 \times 12 \times 12$ grid for optical property calculations. HSE06 calculations were carried out using a $4 \times 4 \times 4$ *k*-point mesh with a reduced plane-wave cutoff of 500 eV, following standard practice for computationally demanding hybrid-functional calculations. The energy convergence criterion for the SCF cycles was 2.0×10^{-5} eV per atom. The electronic ground state was determined by iterating to self-consistency using the Ensemble Density Functional Theory (EDFT) minimization scheme. To assess mechanical stability, the elastic constants of the relaxed Sr_3NF_3 structure were calculated using the finite-strain method as implemented in CASTEP.[28] Band-edge positions relative to redox potentials were estimated using Mulliken electronegativity. We note that a more precise determination of absolute band-edge positions would require slab models and vacuum-level alignment, which are beyond the scope of the current study focused on intrinsic bulk properties. The effective masses (m^*) were calculated from the curvature of the band edges, which was determined by fitting the E–k dispersion relation to a parabolic function. The second

derivative (d^2E/dk^2) was then obtained numerically from the fitted curves, and m^* was calculated by using eqn (1)[29]

$$m^* = \hbar^2 \left(\frac{d^2E}{dk^2} \right)^{-1} \quad (1)$$

3. Results and discussion

3.1 Structural properties

As shown in Fig. 1(a), Sr_3NF_3 adopts a cubic structure, which is characterized by the $Pm\bar{3}m$ space group (#221). Sr_3NF_3 unit cell has seven atoms consisting of three strontium (Sr), one nitrogen (N) and three fluorine (F) atoms. This compound follows A_3BX_3 formula of perovskite structures, where A is cation and B and X are anions. In Sr_3NF_3, A is Sr, B is N and X is F. The positions of atoms in this configuration are Sr at 3d (0.5, 0, 0), N at 1a (0, 0, 0) and F at 3c (0.5, 0.5, 0). The 3D polyhedral view and stoichiometric ac plane of Sr_3NF_3 are shown in Fig. 1(b) and (c). Sr_3NF_3 crystal structure features distorted SrF_4N_2 octahedra, with Sr^{2+} at the center coordinated by four equatorial F^- and two axial N^{3-} anions. These octahedra are corner-connected, forming a robust 3D ionic network. The mixed-anion coordination induces geometric and electronic asymmetry, which is functionally significant for tuning optoelectronic and photocatalytic properties. The obtained value of lattice parameter and bandgap exhibits close agreement with the theoretical data previously documented, as shown in Table 1. The strain-induced structural parameters were studied by applying strain ranging from −6% to +6% with a step of 2%. The respective lattice parameters were adjusted according to applied strain by using the formula in eqn (2):

$$\% \, \varepsilon = \frac{a_s - a_i}{a_i} \times 100\% \quad (2)$$

Here, ε denotes the applied strain, while a_s and a_i are the respective lattice constants for the strained and intrinsic systems. Table 2 summarizes the calculated unit cell volume and lattice constants for the unstrained and biaxially strained Sr_3NF_3 structures, as obtained after full structural optimization. Applying strain significantly affects the structural parameters of Sr_3NF_3. The unit cell volume reduces (increases) under compressive (tensile) strain as seen in Table 2. Table 2 also gives the cohesive energy (ΔE_{coh}) of the strained and unstrained structures, which was evaluated through the following eqn (3):

$$\Delta E_{coh}(Sr_3NF_3) = \frac{[E_{total}(Sr_3NF_3) - 3E_{Sr} - E_N - 3E_F]}{N} \quad (3)$$

Here, E_{Sr}, E_N and E_F correspond to the reference atomic energies of Sr, N and F atoms and E_{total} is the total energy of the Sr_3NF_3 structure. The calculated cohesive energies are negative for both

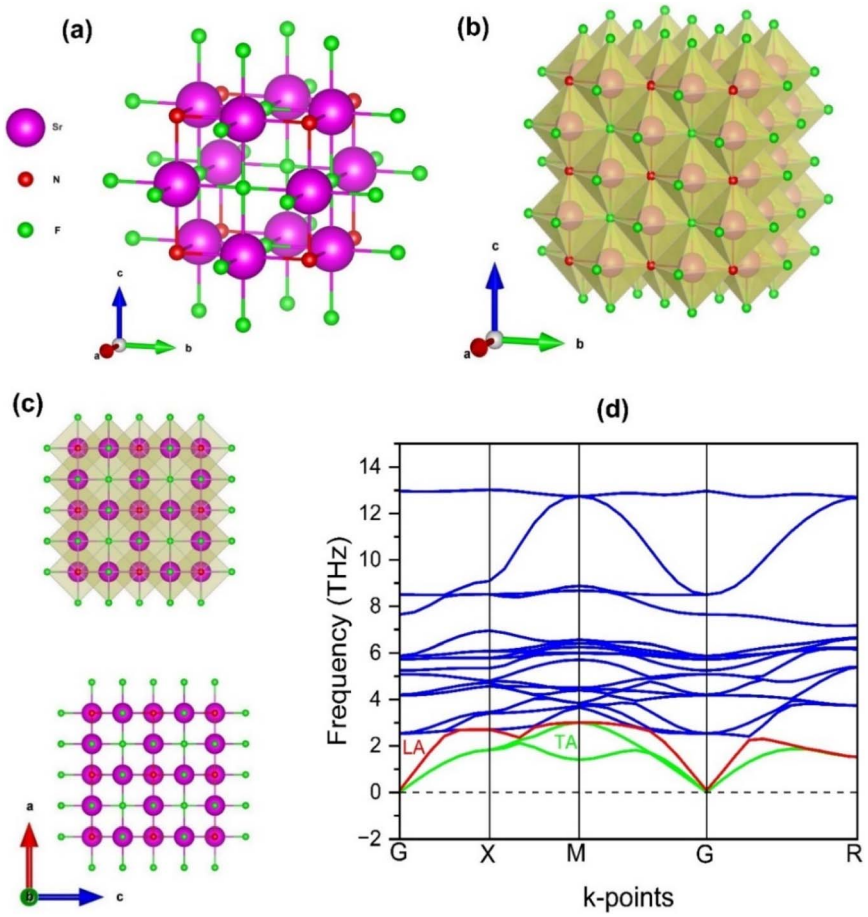

Fig. 1 Structural and vibrational properties of Sr_3NF_3 (a) ball-and-stick model, (b) 3D-polyhedral view, (c) ac-plane projection in ball-stick model (bottom) and polyhedral (top) and (d) phonon dispersion curve.

Table 1 The previously reported and calculated lattice parameter (Å) and band gap (eV) of Sr_3NF_3

	Lattice parameter (Å)		Bandgap (eV)	
Structure	This study	Previous study	This study	Previous study
Sr_3NF_3	5.1629	5.19 (ref. 30)	1.33 (PBE), 2.06 (HSE)	2.17 (HSE)[30]

Table 2 Obtained values of lattice parameters for unstrained and strained Sr_3NF_3

Applied strain (%)	Unit cellvolume, V (Å^3)	Lattice constants, $a = b = c$ (Å)	Cohesive energy, E_{coh} (eV per atom)
−6	114.3	4.85	−5.34
−4	121.75	4.95	−5.43
−2	129.52	5.06	−5.48
0	137.62	5.16	−5.47
+2	146.04	5.26	−5.48
+4	154.8	5.37	−5.45
+6	163.9	5.47	−5.40

strained and unstrained Sr_3NF_3, confirming the exothermic formation feasibility under both conditions.

Phonon dispersion gives us information about how phonon frequencies change with wave vector, which is crucial for knowing a material's thermal conductivity, heat capacity and elasticity. Negative eigen frequencies in the phonon curve are indicators of dynamic instability and energetically unfavored vibrational modes, which possibly may result in lattice deformation or structural failure.[31] The dynamic stability of Sr_3NF_3 is confirmed by the phonon dispersion curve in Fig. 1(d), as there are no negative frequencies throughout the entire Brillouin zone. Additionally, the phonon spectrum has 21 branches: 3 acoustic and 18 optical modes. This is consistent with a unit cell with 7 atoms. The red curve indicates the longitudinal acoustic (LA) and green curves indicate the two transverse acoustic (TA) modes, which have zero frequency at the G point and exhibit linear dispersion corresponding to 3D stable crystal. They control the low-temperature vibrational behavior of the lattice and are crucial to characterizing mechanical stiffness and thermal conductivity. The lack of any anomalous behavior around the G point additionally supports the mechanical and structural robustness of Sr_3NF_3, verifying its applicability in photocatalytic and thermally challenging applications.

Electron localization function (ELF) plots, which reveal information on the electron distribution, are employed to describe the chemical bonding, where covalent and ionic characteristics can be determined from shared or localized electron densities, respectively. Fig. 2 depicts the ELF plots of Sr_3NF_3 in the (100) and (200) planes, representing high and low electron concentration with a blue-to-red color scheme. The (100) plane was selected because it slices directly through the key Sr–N and Sr–F bonding environments, giving a clear view of the mixed-anion framework. To complete the picture, the (200) plane, a parallel slice deeper into the crystal was analyzed to visualize the charge redistribution from a bulk perspective. In (100) plane we see overlapping of charges between Sr and N atoms, suggesting covalent bond between Sr–N. The charge distribution of (200) plane reveal that Sr–F form ionic bonds as the charge boundaries of Sr and F are not aligned. Overall, the stability of the Sr_3NF_3 crystal is primarily attributed to strong

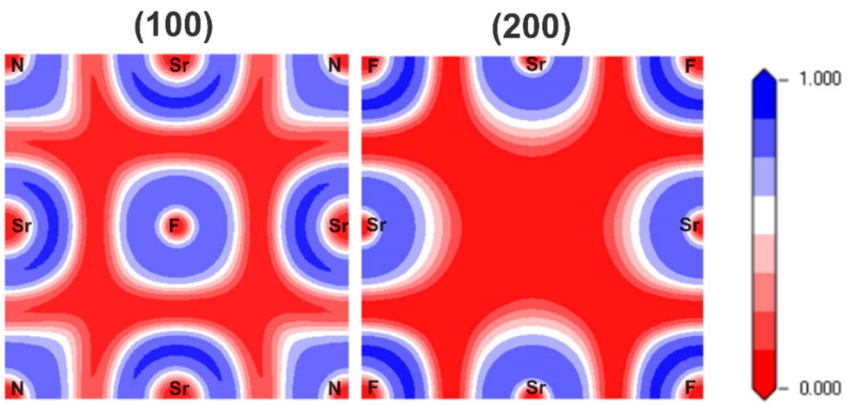

Fig. 2 ELF plot of Sr_3NF_3 in the (100) and (200) crystallographic planes.

ionic bonding, with secondary covalent contributions from Sr–N interactions. These ELF planes are not intended to represent active redox surfaces, but rather to illustrate intrinsic bulk bonding asymmetry and internal polarization, which play a critical role in governing the mechanical, optical and electronic properties of perovskite materials relevant to photovoltaics, LEDs and photocatalysis.

3.2 Electronic properties

3.2.1 Band structure and density of states. The analysis of a perovskite's band structure is essential for photocatalytic applications to verify that it possesses the direct and optimal bandgap required to enable strong light absorption and effective charge carrier generation.[32] The lower-energy valence band emerges in the negative part and the conduction bands with higher-energy states appear in the positive part of Fig. 3(a). The energy separation between both bands indicates bandgap (E_g). The black dashed line at zero eV indicates Fermi level (E_F), which is a key reference point in the study of electronic properties in semiconductor physics. The alignment of the valence band maximum (VBM) and conduction band minimum (CBM) at the same *k*-point can result in a direct bandgap.[33] It is an important characteristic of optoelectronic materials and allows the strong absorption of photons by conserving momentum in the electronic transitions.[34] Fig. 3 shows band structure diagram of Sr_3NF_3, where electron energy is represented in the *y*-axis through −4 eV to 4 eV against the high symmetric G–X–M–G–R paths of Brillouin zone in the *x*-axis. The calculations reveal that Sr_3NF_3 has a direct bandgap located at the G-point. This finding is confirmed by two separate methods: the GGA-PBE functional, giving a bandgap of 1.33 eV and HSE06 hybrid functional, giving more wider value of 2.06 eV. Although experimental data are not yet available for Sr_3NF_3, HSE06 has been shown to reproduce experimental bandgaps of halide and mixed-anion perovskites with significantly higher accuracy than the GGA-PBE functional, which is known to systematically underestimate bandgaps. A comparative summary of experimental and calculated bandgaps using PBE and HSE06 for related perovskites is provided in the SI (Table S1). The corresponding dispersion curves for the HSE06 (blue lines) and GGA-PBE (red lines) calculations are presented in Fig. 3.

By describing the distribution of electronic or vibrational states as a function of energy, the density of states (DOS) reveals the key electronic characteristics of a material.[35] It describes how electrons fill energy bands and how materials behave under applied external conditions, whether light or electric fields. The total DOS gives contribution of all orbitals and the partial DOS (PDOS) splits up that contribution, showing how much each species and each type of orbital contributes, helping reveal the states that dominate the material's band edge, determining its electronic behavior.[36] The DOS and PDOS of Sr_3NF_3 are shown in Fig. 3(a). The analysis indicates that N 2p and Sr 3d orbitals dominate valence band regions, while Sr 3d orbitals dominate conduction band states. The PDOS indicates that N 2p orbitals mainly contribute VBM and the CBM is primarily composed of Sr 5s orbitals.

To further explain the character of the band edges, band decomposed charge density plots of VBM and CBM is shown in Fig. 3(b). The VBM charge density is mainly localized around N atoms. This confirms VBM is dominated by N-2p orbitals. The CBM exhibits a more delocalized distribution over Sr atoms,

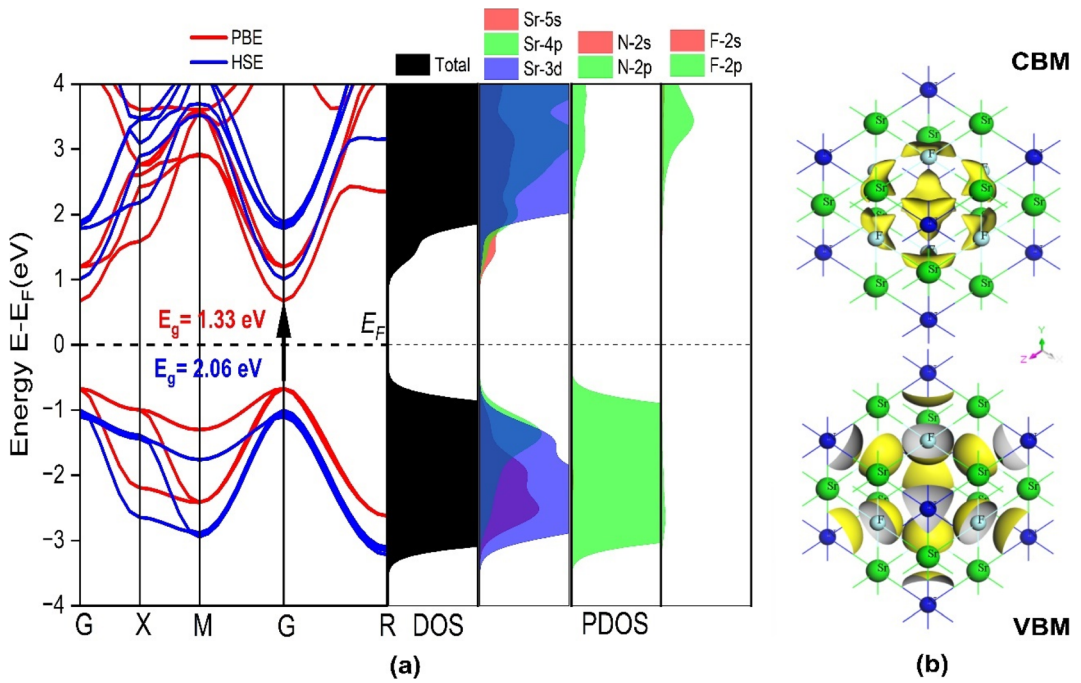

Fig. 3 (a) Band structure using GGA-PBE and HSE06 along with DOS & PDOS using GGA-PBE of unstrained Sr_3NF_3. (b) Charge density isosurfaces of the CBM (top) and VBM (bottom) for Sr_3NF_3.

arising mainly from Sr-5s orbitals. This spatial separation of hole and electron states is favorable for charge transport and suppresses electron–hole recombination, which is beneficial for photocatalytic applications.

3.2.2 Strain effects on band structure and density of states. Fig. 4 shows the band structures of Sr_3NF_3 under strain. The corresponding strain-induced changes in bandgap values are listed in Table 3. Compressive strain resulted in a larger bandgap by approximately 1.048 times than that of the unstrained system, whereas tensile strain led to a bandgap that was reduced by roughly 1.16 times than the unstrained bandgap, demonstrating that the bandgap was sensitive to strain. The reasons behind this behavior are that applying strain modifies the spacing and tilt of crystal bonds, particularly within the octahedral frameworks of perovskites. Compressive strain shortens bond lengths, enhancing orbital overlap and lifting band-edge energies, thereby increasing the bandgap. In contrast, tensile strain lengthens these bonds, reducing overlap and narrowing the bandgap.[37] Sr_3NF_3 has a direct bandgap in the strained as well as unstrained conditions which is advantageous for enhanced photon absorption, a key requirement for photocatalytic efficiency. The materials with bandgaps between

Table 3 Strain dependent bandgap values of Sr_3NF_3

Strain (%)	GGA-PBE (eV)	HSE06 (eV)
−6%	1.31	2.16
−4%	1.46	2.12
−2%	1.40	2.07
0%	1.33	2.06
+2%	1.26	1.94
+4%	1.18	1.86
+6%	1.09	1.77

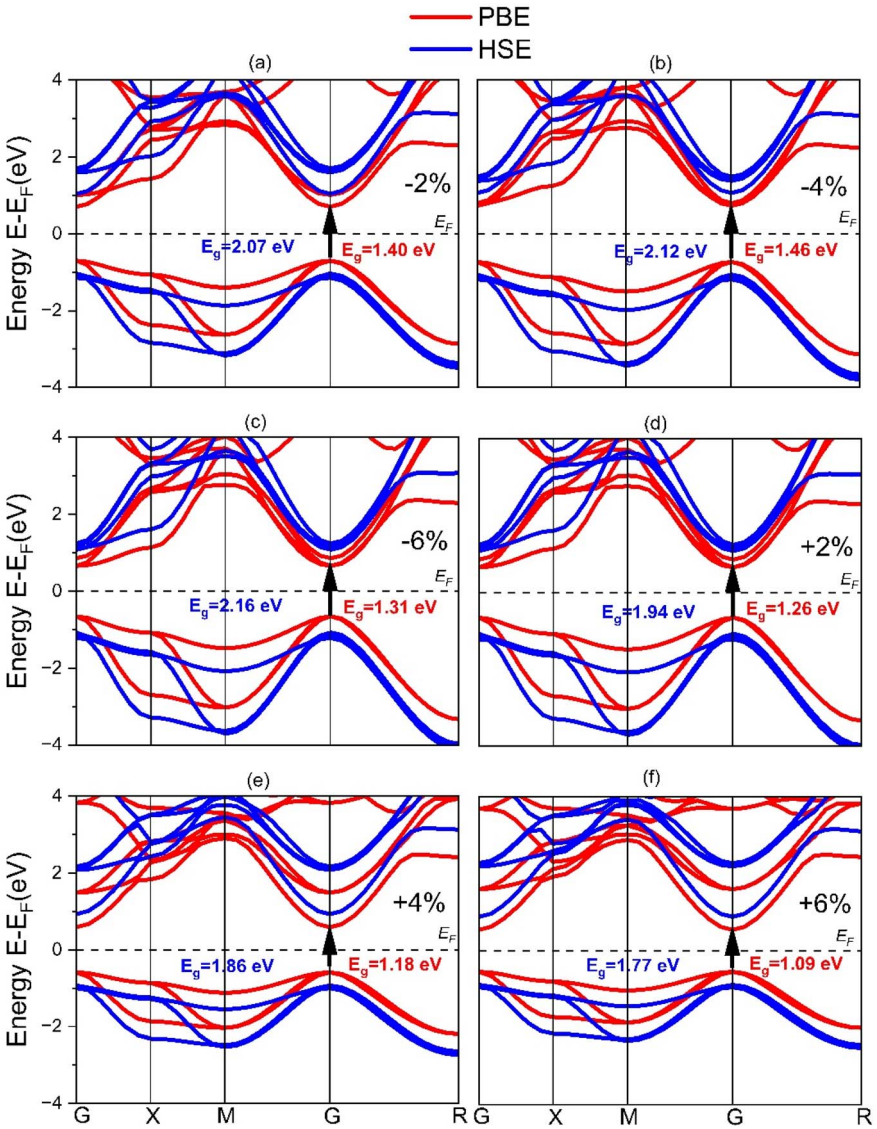

Fig. 4 Electronic band structures of Sr_3NF_3 with various strains: (a) −2%, (b) −4%, (c) −6%, (d) +2%, (e) +4% and (f) +6% calculated using HSE06 (blue) and GGA-PBE (red) functional.

1 to 3 eV are considered ideal for visible-light-driven photocatalysis, as they can efficiently harness a broad part of the solar radiation.[38] Thus, the strain-versatility of Sr_3NF_3 makes it a potential material for solar-driven water splitting and other photocatalytic applications.

The PDOS for Sr_3NF_3 with various strains are depicted in Fig. 5. The character of the VBM is consistent for all the conditions, originating mainly from N 2p orbitals. But the composition of CBM has a strong dependence on the strain. For compressive strains, Sr 3d orbitals mainly contribute the CBM. But for tensile strain, CBM is dominated by Sr 5s orbital, which causes the bandgap to reduce.

3.2.3 Electron density difference. Electron density difference (EDD), denoted as ($\Delta\rho$), which illustrates the redistribution of electrons upon bond formation, is calculated using eqn (4) given below:[39]

$$\Delta\rho = \rho_{Sr_3NF_3} - 3\rho_{Sr} - \rho_N - 3\rho_F \quad (4)$$

Here, $\rho_{Sr_3NF_3}$ represents the total charge density of the optimized Sr_3NF_3 crystal, while ρ_{Sr}, ρ_N and ρ_F are the respective charge densities of the individual isolated atoms. Fig. 6 presents two-dimensional (2D) sectional EDD plots for the (100) and (200) planes together with three-dimensional (3D) volumetric EDD visualizations of Sr_3NF_3. The red and blue areas denote charge accrual and deficit, respectively. The 2D EDD plots along the (100) and (200) planes clearly show that electron density is transferred from Sr atoms to the more electronegative N and F atoms. Charge accumulation is observed around N and F due to their high electronegativity, while electropositive Sr atoms donate electrons, resulting in pronounced charge depletion around Sr. To provide a more intuitive spatial description of this redistribution, the 3D volumetric EDD visualization highlights Sr-centered coordination environments, where electron depletion around Sr and electron accumulation on surrounding N and F anions are clearly evident. This Sr-centered electron depletion indicates hole accumulation at the Sr sites, which are

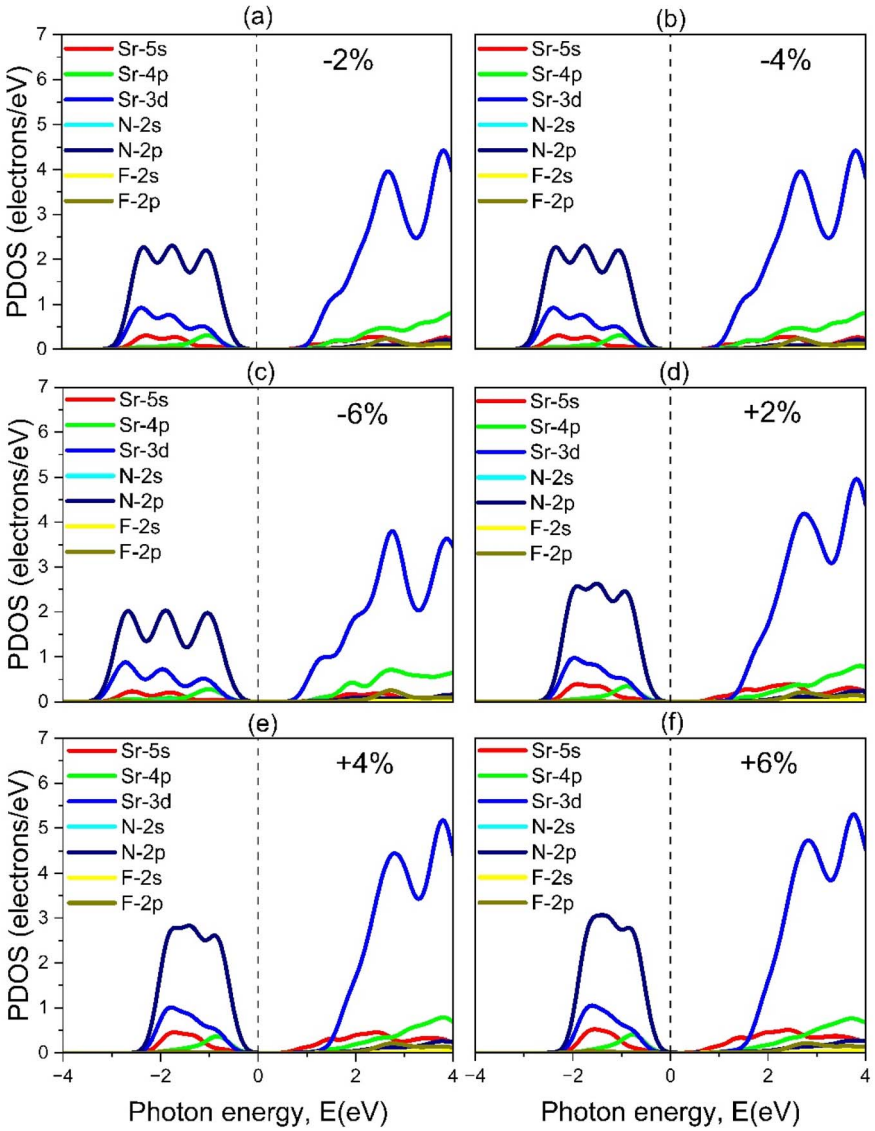

Fig. 5 PDOS of Sr_3NF_3 under various strain conditions: (a) −2%, (b) −4%, (c) −6%, (d) +2%, (e) +4% and (f) +6%.

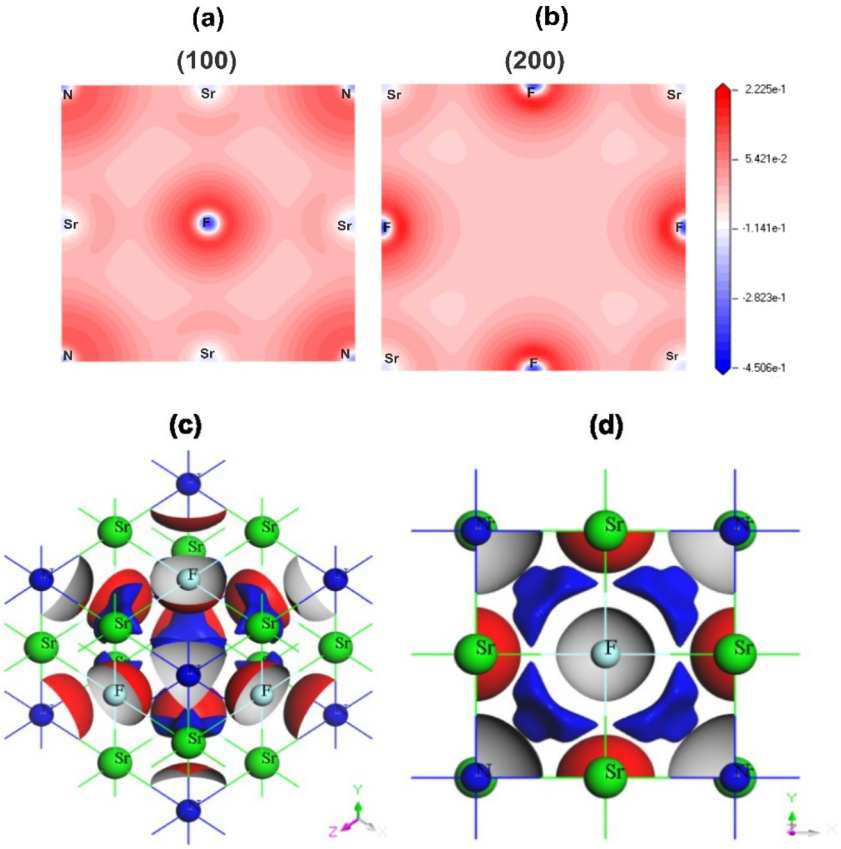

Fig. 6 Electron density difference (EDD) plots of Sr_3NF_3 showing (a and b) 2D contours for the (100) and (200) planes and (c and d) 3D volumetric visualizations.

widely recognized as the primary oxidation centers in photocatalytic OER. The mixed N–F coordination around Sr facilitates strong internal polarization and charge separation, which are beneficial for hole-driven surface oxidation processes. These 2D and 3D EDD representations are intended to illustrate the intrinsic electronic environments associated with OER-relevant oxidation centers, rather than explicit surface slab models.

To complement the EDD analysis, Mulliken and Hirshfeld charge analyses of Sr_3NF_3 were performed to provide a quantitative description of charge transfer. The results are shown in Table 4, where the net loss of electrons is represented by a positive number, while the net gain is shown by a negative value. The Mulliken analysis indicates that Sr atoms donate approximately 0.88 e each, while N and F atoms gain -0.89 e and -0.58 e, respectively, confirming substantial electron transfer from Sr to the anions. Hirshfeld analysis yields smaller but consistent charge values, with Sr carrying +0.42 e, N -0.58 e, and F -0.23 e, reflecting the more conservative nature of this partitioning scheme. These results support the EDD results, which show charge accumulation around N and F and depletion around Sr. The observed charge transfer from Sr to the N and F atoms suggests strong internal polarization and charge separation. This is favorable for photocatalysis, as it may help reduce charge carrier recombination and promote surface redox reactions.[40]

3.2.4 Effective masses and redox potential. The photocatalytic activities of a material are heavily influenced by effective mass of charge carriers, since it directly affects their mobility as well as separation and recombination rates.[41] The effective masses of both the strained and unstrained structures of Sr_3NF_3 were calculated. Electron effective masses (m_e^*) were evaluated at the CBM, while the valence band heavy-hole region was used to determine the hole effective masses (m_{hh}^*). As summarized in Table 5, m_{hh}^* is higher than m_e^*, indicating hole dominated transport behavior. Consistently, the calculated Fermi level (-5.94 eV w.r.t vacuum) lies closer to the valence band edge (VBE) (-6.72 eV) than to the conduction band edge (CBE) (-4.66 eV), indicating a p-type transport tendency in pristine Sr_3NF_3. m_e^* and m_{hh}^* in Sr_3NF_3 show clear strain-dependent behavior. At 0% strain, m_e^* is 0.430 m_0 and m_{hh}^* is 0.859 m_0, yielding a mass ratio ($D = m_{hh}^*/m_e^*$) of 1.99. At compressive strain of -6%, m_e^* increases to 0.626 m_0, while m_{hh}^* is 0.684 m_0, resulting in a relatively low mass ratio $D = 1.093$.

Table 4 Computed Mulliken and Hirshfeld atomic charges for Sr_3NF_3

Species	Mulliken charge (e)	Hirshfeld charge (e)
N	−0.89	−0.58
F	−0.58	−0.23
Sr	0.88	0.42

This suggests that compressive strain reduces the difference in carrier mobilities, which may increase electron–hole recombination rate. In contrast, tensile strain of +6% leads to a slight increase of m_e^* to 0.434 m_0, but m_{hh}^* rises more substantially to 1.201 m_0, which gives a much higher $D = 2.766$. This increased asymmetry in carrier effective masses under tensile strain favors spatial charge separation. This effect suppresses recombination and enhances photocatalytic activity. In all cases, m_e^* and m_{hh}^* of Sr_3NF_3 are considerably smaller than those found in conventional photocatalysts like Fe_2O_3,[42] In_2O_3,[43] and TiO_2.[44] These low effective mass values indicate that photogenerated holes and electrons can travel more rapidly to surface-active sites, which may be responsible for a greater efficiency in redox reactions.[45] Additionally, the deviation of D from unity signifies a large mismatch between hole and electron mobility. This facilitates the separation of charges and decreases recombination rate of holes and electrons. Taken together, its potential for high carrier mobility and excellent charge separation suggests that Sr_3NF_3 can be a promising candidate for photocatalysis.

The electronic band edge alignment of Sr_3NF_3 structures is depicted in Fig. 7. The CBE denotes the minimum energy level accessible to excited electrons, whereas the VBE signifies the highest energy level occupied by electrons under equilibrium conditions. These band edge energy levels, which are critical for determining photocatalytic activity, were computed using the following formulas in eqn (5) and (6):[46]

$$E_{CBE} = X - \frac{E_g^{HSE06}}{2} \quad (5)$$

$$E_{VBE} = X + \frac{E_g^{HSE06}}{2} \quad (6)$$

Here, X denotes geometric mean of Mulliken electronegativity values for the constituent atoms. E_g^{HSE06} refers to the HSE06 bandgap of the Sr_3NF_3 structure. The computed value of X for Sr_3NF_3 is approximately 5.69 eV.

Fig. 7 shows the calculated energy levels of CBE and VBE with respect to the vacuum level of Sr_3NF_3 under different strain conditions. These are compared with standard redox potential for water splitting (H^+/H_2 reduction and H_2O/O_2 oxidation) at neutral (pH = 7) and acidic (pH = 0) conditions. For photocatalytic hydrogen (oxygen) production to occur, the CBE (VBE) of the material must lie higher (lower) than the proton (water) reduction (oxidation) level. For both unstrained and strained conditions, the CBE of the material lie below proton reduction potential (H^+/H_2), which is ~−4.03 eV at pH 7 and ~−4.44 eV at pH = 0, with respect to vacuum. The conduction band electrons of Sr_3NF_3 lack the necessary energy to facilitate the reduction of protons to hydrogen. For both strained and unstrained conditions the VBE of Sr_3NF_3 is significantly below the water oxidation potential (H_2O/O_2), which is ~−5.26 eV at pH 7 and ~−5.67 eV at pH = 0. This means that the photogenerated valence band holes are sufficiently oxidizing to facilitate the OER, enabling conversion of water to oxygen.

Table 5 Strain dependent m_e^* and m_{hh}^* in Sr_3NF_3, expressed relative to the electron rest mass (m_0) and mass ratio, $D = m_{hh}^*/m_e^*$

Strain (%)	m_e^*	m_{hh}^*	D
−6%	0.626	0.684	1.093
−4%	0.501	0.798	1.592
−2%	0.430	0.757	1.758
0%	0.430	0.859	1.997
+2%	0.431	0.965	2.236
+4%	0.432	1.081	2.498
+6%	0.434	1.201	2.766

To quantify this oxidizing capability, the Kinetic Overpotential (KOP) was calculated. KOP represents the thermodynamic driving force available for OER and is defined as the energy difference between VBE and water oxidation potential. It is expressed by eqn (7):

$$KOP_{OER} = |E_{VBE} - E_{H_2O/O_2}| \quad (7)$$

The unstrained Sr_3NF_3 has a KOP of 1.43 eV and 0.99 eV at pH 7 and pH 0, respectively. Under increasing compressive strain from −2% to −6%, KOP rises steadily, reaching a maximum of 1.51 eV (pH 7) and 1.07 eV (pH 0) at −6% strain, indicating an enhanced intrinsic oxidizing tendency of the valence band holes. In contrast, tensile strain from +2% to +6% reduces the KOP values, with the lowest observed at +6% strain: 1.32 eV (pH 7) and 0.88 eV (pH 0). These values reflect a strain tunable thermodynamic driving force for OER, with compressive strain providing the greatest intrinsic overpotential (1.51 eV at pH 7). Notably, these overpotentials are comparable to or higher than those reported for conventional OER photocatalysts such as $BiVO_4$ (~0.87 eV),[47] TiO_2 (~1.55 eV),[48] Fe_2O_3 (~1.72 eV),[49] TaON (~0.92 eV).[50]

It should be noted that the KOP values discussed here are derived from bulk band-edge alignment and represent an intrinsic electronic oxidation driving force. A full kinetic evaluation of OER would require explicit surface free-energy calculations of reaction intermediates, which are beyond the scope of the present bulk-focused study.

Although Sr_3NF_3 may be unsuitable for overall water splitting unless paired with complementary photocatalyst or co-catalyst, it can be incorporated into Z-scheme photocatalytic systems or type-II heterojunctions, where it functions as the potential OER-active component. In such architectures, Sr_3NF_3 would primarily contribute oxidative driving force, while a secondary material with a more negative conduction band facilitates hydrogen evolution. Additionally, the promising oxidizing potential of the photogenerated holes in Sr_3NF_3 under visible light irradiation suggests possible applicability in degrading refractory organic compounds. These persistent pollutants may be degraded to simpler, biodegradable intermediates and, eventually, to carbon dioxide and water.

3.3 Optical properties

A detailed evaluation of Sr_3NF_3 perovskite's optical properties is conducted in this section to determine its potential for photocatalytic applications.

3.3.1 Dielectric functions. The dielectric function, consisting of real and imaginary parts, plays a crucial role in

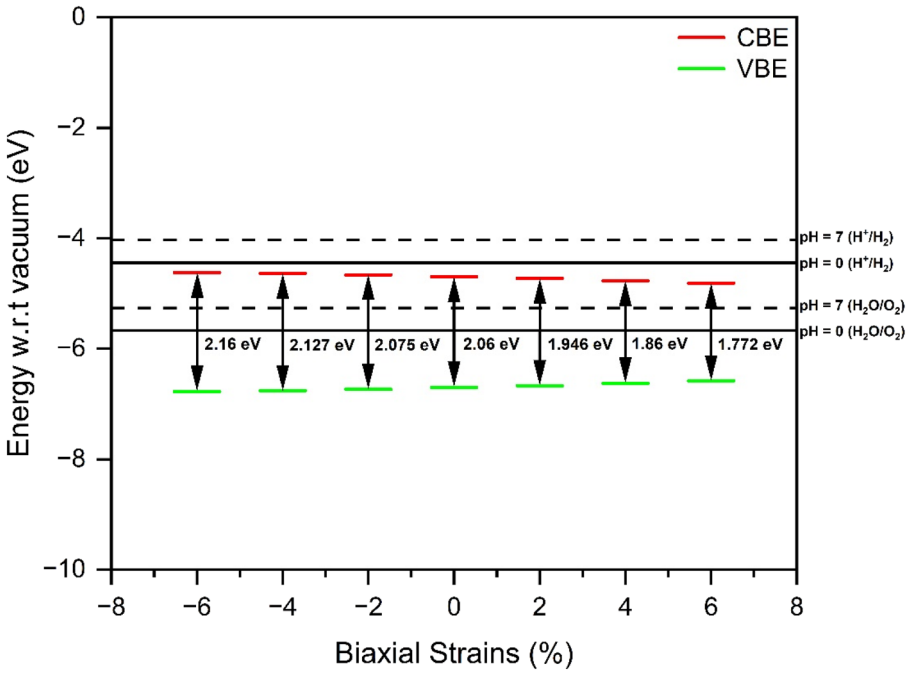

Fig. 7 Photocatalytic band edges of strained and unstrained Sr_3NF_3.

determining a material's light absorption behavior and its internal charge carrier response.[51] Dielectric function's real component, $\varepsilon_1(\omega)$, illustrated in Fig. 8(a), is calculated using the Kramers–Kronig relations given by eqn (8):[52]

$$\varepsilon_1(\omega) = 1 + \frac{2}{\pi} P \int_0^{\infty} \frac{\omega' \varepsilon_2(\omega')}{\omega'^2 - \omega^2} d\omega' \quad (8)$$

$\varepsilon_1(\omega)$ of Sr_3NF_3 perovskite can be controlled by applying biaxial strain. An enhancement (reduction) of the main dielectric peak is noticed as the structure experiences a higher compressive (tensile) strain, along with a red (blue) shift towards lower (higher) energy. The static dielectric constant $\varepsilon_1(0)$ can be obtained using $\varepsilon_1(\omega)$, when evaluated at the point where the photon energy approaches zero.[53]

The static dielectric constant of unstrained Sr_3NF_3 is 3.64, as shown in Fig. 8(a). However, when compressive strain is applied, this value steadily increases. In particular, 3.73, 3.87 and 4.11 are the static dielectric constants of −2%, −4% and −6% strained structures, respectively. For tensile strain the static dielectric constants are 3.59, 3.58 and 3.6 for +2%, +4% and +6% strained structures, respectively. The strain-dependence of the dielectric function of Sr_3NF_3 can be understood from changes in electronic polarizability and interband transition strength induced by lattice distortion. Compressive strain reduces the interatomic Sr–N and Sr–F bond lengths. This bond contraction enhances the overlap between Sr 3d/5s and N 2p orbitals, effectively reducing the energy required for electronic polarization. Additionally, the PDOS of Sr_3NF_3 reveals that compressive strain shifts the CBM character from Sr 5s orbitals toward Sr 3d orbitals, which lie at lower energies and thus couple more strongly with N 2p valence band states, thereby increasing the material's polarizability and static dielectric constant. This results in a redshift and enhancement of the dielectric response. Conversely, tensile strain weakens orbital overlap, reducing polarizability and causing a blueshift with diminished intensity. The analysis reveals that the maximum static dielectric constant is achieved in the Sr_3NF_3 structure when subjected to 6% compressive strain. Large value of static dielectric constant reduces the Coulomb attraction between electron and hole.[54] This gives rise to a small exciton binding energy and free carriers are easier to form.[55] As a result, the weaker interaction between free carriers diminishes their recombination rate.[56] Consequently, a high dielectric constant is a critical element for attaining efficient charge separation and collection in photocatalytic applications.

The imaginary part $\varepsilon_2(\omega)$, characterizes the material's light absorption, which arises due to electronic transitions from occupied states to higher energy levels.[57] The bandgap (E_g) determines the low-energy cut-off for these transitions.[58] It is shown in Fig. 8(b) and can be represented by eqn (9):[59]

$$\varepsilon_2(\omega) = \frac{2e^2\pi}{\Omega\varepsilon_0} \sum_{k,v,c} \left|\psi_k^c \left| \hat{U} \cdot \vec{r} \right| \psi_k^v\right|^2 \delta\left(E_k^c - E_k^v - E\right) \quad (9)$$

The Sr_3NF_3 perovskite shows substantial optical absorption, approximately in the range 2–5 eV. Notably, the positions and intensities of these absorption characteristics can be tuned by applying strain. When compressive strain is applied redshift is observed along with an increase of absorption peaks. Conversely, applying tensile strain causes the optical absorption to move to higher photon energies (blueshift) accompanied with reduction of intensity. Similar strain-induced optical trends have been reported in other mixed-anion perovskites and

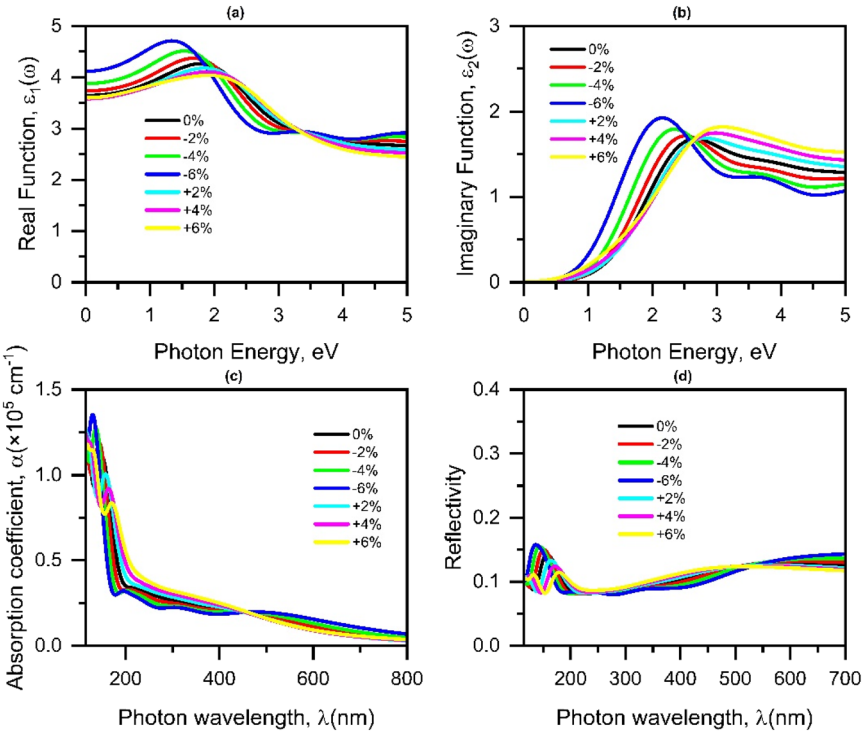

Fig. 8 Strain effects on optical properties of Sr_3NF_3. (a) Real and (b) imaginary dielectric function *vs.* photon energy. (c) Absorption coefficient and (d) reflectivity *vs.* wavelength.

oxynitrides, such as $SrTaO_2N$,[60] Ca_3PI_3,[61] and Sr_3AsI_3.[62] This adds to the evidence that strain can engineer the band gap and adjust absorption in the material. Note that the optical absorption onset corresponds to the PBE bandgap (1.33 eV) rather than the HSE06 value, as optical properties were calculated using the PBE functional. The minor tail observed below this energy is a consequence of the Gaussian smearing (0.5 eV) applied to broaden the spectra, not defect states.

3.3.2 Absorption. A perovskite material's efficiency in capturing incident solar radiation is determined by its absorption coefficient. A higher absorption coefficient is desirable for photocatalytic applications, as it allows the material to generate more free carriers to drive the chemical reactions. Fig. 8(c) depicts the absorption coefficient of Sr_3NF_3 with respect to wavelength, which can be expressed as eqn (10):[63]

$$\alpha(\omega) = \left[\sqrt{{\varepsilon_1}^2(\omega) + {\varepsilon_2}^2(\omega)} - \varepsilon_1(\omega)\right]^{1/2} \quad (10)$$

Sr_3NF_3 exhibits strong light absorption of $\sim 1.1 \times 10^5\ cm^{-1}$ at 150 nm in the ultraviolet (UV) region. Under compressive strain (−6%), the absorption further increases to about $1.35 \times 10^5\ cm^{-1}$ at 130 nm, which is ~1.21 times greater than the absorption of unstrained structure. This enhancement originates from coupled electronic-structure effects induced by lattice compression. Specifically, the conduction band minimum evolves from predominantly Sr-5s character in the unstrained configuration to Sr-3d character under compressive strain, which increases the joint density of states and enables additional optical transitions from N-2p valence states. At the same time, the imaginary part of the dielectric function, $\varepsilon_2(\omega)$, becomes broader and more intense, indicating an increased density and oscillator strength of allowed interband transitions. From a photocatalytic carrier-generation perspective, these effects promote more efficient generation of electron–hole pairs under UV illumination by increasing both photon absorption probability and transition strength, thereby enhancing the population of photogenerated carriers available for surface redox reactions. As a result, compressively strained Sr_3NF_3 is particularly favorable for UV-driven photocatalytic processes. In the visible region, unstrained Sr_3NF_3 shows an absorption coefficient of $\sim 0.25 \times 10^5\ cm^{-1}$ at around 320 nm. Notably, tensile strain improves absorption in the visible spectrum while simultaneously reducing it in the UV region owing to bandgap narrowing. At a tensile strain of +6%, the absorption coefficient increases to $\sim 0.37 \times 10^5\ cm^{-1}$ at 320 nm, representing a ~1.48 times improvement over the unstrained structure. These findings indicate that applying strain is a viable approach to tailoring the optical absorption properties of Sr_3NF_3 for specific photocatalytic applications. Although the visible-light absorption coefficient of Sr_3NF_3 is lower than that in the UV region, its magnitude is still comparable to that of several widely studied photocatalysts and mixed-anion oxynitrides. A quantitative comparison is provided in Table S3 (SI).

3.3.3 Reflectivity. The reflectivity of Sr_3NF_3 with respect to wavelength under various strains is depicted in Fig. 8(d) and can be expressed as eqn (11):[64]

$$R(\omega) = \frac{(1-n)^2 + k^2}{(1+n)^2 + k^2} \quad (11)$$

Sr_3NF_3 exhibits low reflectivity of around 10% at a wavelength of 320 nm across all strain conditions, indicating minimal reflection in the visible region. This low reflectivity is advantageous for light-harvesting applications such as photocatalysis, as it allows more incident light to be absorbed. In the ultraviolet (UV) region, a noticeable reflectivity peak is observed, with the unstrained Sr_3NF_3 reaching a value of ~14% at 150 nm. Under 6% compressive (tensile) strain, this peak increases (decreases) to ~15.8% (~11.4%) at a slightly shifted wavelength of 137 (180) nm, suggesting the strain tunability of reflectivity in the UV region.

3.3.4 Refractive index. It can be expressed as eqn (12):[65]

$$\eta(\omega) = \left[\frac{\sqrt{\varepsilon_1{}^2(\omega) + \varepsilon_2{}^2(\omega)}}{2} + \frac{\varepsilon_1(\omega)}{2}\right]^{1/2} \quad (12)$$

The real (η_1) and imaginary (η_2) part of refractive index of Sr_3NF_3 for the unstrained structure and under various applied strains is shown in Fig. 9(a) and (b), respectively. It is found that η_1 exhibits trends closely aligned with those of the real component of the dielectric function, reflecting their intrinsic physical relationship. The static refractive index, $\eta_1(0)$ is highly tunable, varying from approximately 1.9 to 2.1 as the strain is changed from +6% tensile to −6% compressive. This tunability indicates that lattice deformation effectively modifies the electronic polarizability of Sr_3NF_3 by altering orbital overlap and charge distribution within the crystal. The refractive index is consistently higher than unity in all cases confirms that light slows down upon entering the material.[66] This increases the optical path length enhancing light–matter interaction, which promotes greater photon absorption and improves photocatalytic efficiency.[67] The imaginary part of refractive index, η_2 which is also known as the extinction coefficient, $k(\omega)$ is shown in Fig. 9(b). This quantity characterizes photon absorption and follows trends similar to the imaginary part of the dielectric function, $\varepsilon_2(\omega)$. In all the strain states studied, η_2 starts from zero at low photon energies, indicating no significant absorption as there is no allowed electronic transitions, but increases significantly in the visible and UV regions where interband transitions become active. In the visible region, compressive strain shifts the η_2 peaks toward lower photon energies and increases intensity, indicating an increase in allowed optical transitions and absorption. This is due to strain-induced modifications of the band structure, in particular, increased hybridization between N-2p and Sr-derived states, which increases transition probability. Overall, the strain-dependent behavior of both η_1 and η_2 demonstrates that biaxial strain can be used as an effective tool for tailoring the refractive and absorption characteristics of Sr_3NF_3.

3.3.5 Energy loss function. It can be expressed as eqn (13):[68]

$$L(\omega) = \frac{\varepsilon_2(\omega)}{\varepsilon_1(\omega)^2 + \varepsilon_2(\omega)^2} \quad (13)$$

The energy loss function for unstrained and strained Sr_3NF_3 structures is shown in Fig. 9(c). The loss of energy is minimal in the UV and visible range for all structures. This is critical owing to the fact that, in photocatalysis, photo-generated charge carriers (holes and electrons), need to remain energetic long enough with sufficient mobility to reach a surface and perform redox reaction. Low energy loss means that upon excitation electrons can travel longer distances without losing energy, leading to an increased charge carrier lifetime and lower rates of recombination.[69] This process in turn promotes more electrons to the reaction sites, thus enhancing overall photocatalytic performance.

It should be noted that optical transmission spectra were not explicitly calculated in this work. Optical transmission depends on sample thickness and surface morphology, which are not defined within bulk periodic DFT calculations. Therefore, intrinsic optical losses were evaluated using the absorption coefficient, reflectance, refractive index and dielectric response, which are the standard bulk descriptors for photocatalytic materials.

3.4 Mechanical properties

The mechanical properties of Sr_3NF_3 were examined primarily to assess its structural stability under strain, which is relevant for maintaining material integrity during synthesis and operation. The mechanical stability of Sr_3NF_3 structures is determined utilizing the Born stability criteria, which are defined as:[70]

$$C_{11} > 0,\ C_{44} > 0,\ C_{11} + 2C_{12} > 0,\ C_{11} - C_{12} > 0$$

The computed elastic constants across all Sr_3NF_3 configurations satisfy the Born stability requirements for cubic systems, demonstrating the material's mechanical stability as seen in Table 6. These calculated fundamental elastic constants (C_{ij}) were used further to determine the effective bulk moduli (B), shear (G) moduli, Poisson's ratio (ν) and Young's modulus (Y), as given in Table 7. Stiffness and resistance to deformation in a material is indicated by B, G and Y values. The material becomes significantly stiffer and resistant to deformation, as these values increase with compressive strain. Conversely, applying tensile strain softens the material, making it less resistant to both volume and shape changes. The mechanical behavior in terms of brittle and ductile is often assessed with Pugh's (B/G) and Poisson's (ν) ratio. Based on Pugh's criteria, if B/G exceeds the critical threshold of 1.75 material exhibits ductile behavior, which corresponds typically to a ν of about 0.26. The B/G ratios of unstrained and tensile strained structures are less than 1.75, which shows that they are brittle. However, under sufficient compressive strain, the material undergoes a brittle-to-ductile transition. At −4% and −6% strain, the B/G ratios are 2.07 and 2.45, respectively, both considerably higher than the 1.75 value threshold, which indicates ductile behavior. The value of ν increases to 0.32 for compressive strain, while it decreases to 0.12 for tensile strain. This trend in Poisson's ratio agrees with the brittle–ductile transition trend in the B/G ratio analysis. Although high ductility is not a primary operational requirement for stationary

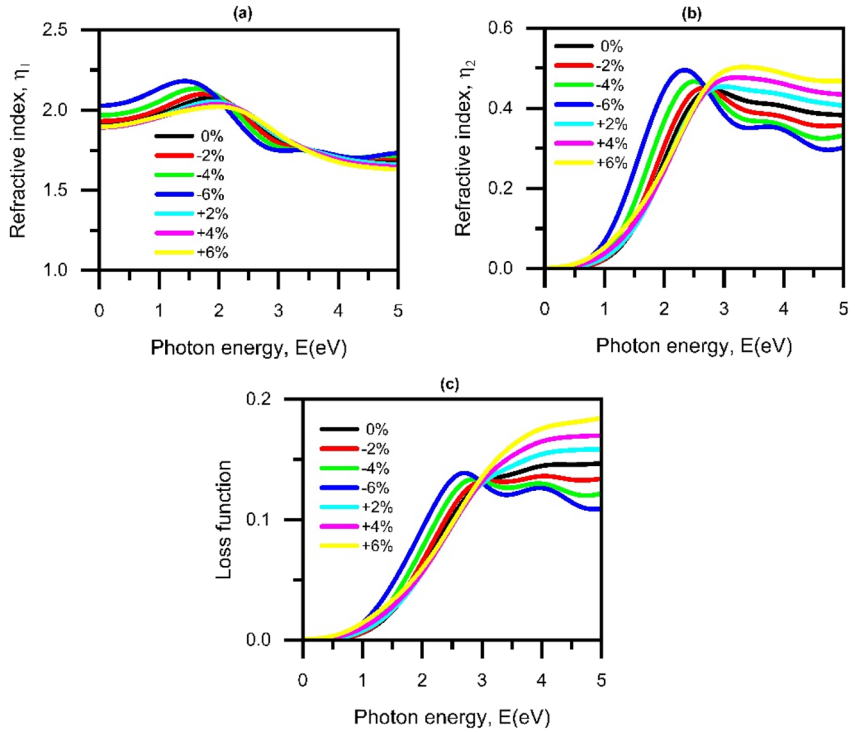

Fig. 9 The obtained optical parameter of Sr_3NF_3 under compressive and tensile strains (a) real and (b) imaginary part of refractive index and (c) energy loss function.

Table 6 Strain-dependent elastic constants C_{ij} (GPa) of Sr_3NF_3

Strain (%)	$C_{11} > 0$	C_{12}	$C_{44} > 0$	$C_{11} + 2C_{12} > 0$	$C_{11} - C_{12} > 0$
−6	282.55	48.81	27.76	380.18	233.73
−4	218.32	39.75	30.78	297.82	178.57
−2	163.24	28.40	32.75	220.05	134.84
0	122.66	23.14	33.60	168.96	99.52
+2	91.84	20.49	33.70	132.84	71.35
+4	66.93	17.23	33.40	101.41	49.69
+6	45.80	13.65	32.42	73.11	32.15

photocatalytic electrodes, this transition indicates enhanced structural sturdiness. It suggests that at the optimal condition for OER, the material is less prone to micro-cracking or mechanical failure during lattice-mismatched film growth and thermal cycling, thereby supporting long-term operational stability.

Table 7 Strain-dependent mechanical properties of Sr_3NF_3, showing the calculated values for B, G, Y, B/G and ν

Strain (%)	B (GPa)	G (GPa)	Y (GPa)	B/G	ν
−6	126.73	51.6	136.49	2.45	0.32
−4	99.27	47.95	123.92	2.07	0.29
−2	73.35	43.93	109.86	1.66	0.25
0	56.32	39.34	95.73	1.43	0.21
+2	44.28	34.483	82.13	1.28	0.19
+4	33.80	29.67	68.8	1.13	0.16
+6	24.37	24.46	54.99	0.99	0.12

4. Conclusions

This work utilizes first-principles calculations to examine the response of Sr_3NF_3 under biaxial strain and to determine its potential applicability in photocatalytic systems. The stability of the material is verified by energetic (negative cohesive energy), dynamic (no imaginary phonon modes) and mechanical (satisfies Born criteria) studies. Sr_3NF_3 has a direct bandgap (2.06 eV with HSE06 and 1.33 eV with GGA-PBE) with a strongly strain-dependent band structure, as compressive strain widens the band gap and tensile strain narrows it. Electron density difference (EDD) plots reveal excellent charge separation driven by internal polarization from its mixed-anion structure. The optical characteristics of Sr_3NF_3 are highly strain dependent, seen by the behavior of its dielectric function, whose main peak redshifts with compression and blueshifts with tension. This tunability is coupled with low reflectivity (~10%) and high absorption capacity of ~1.35×10^5 cm^{-1} (~0.37×10^5 cm^{-1}) in

the ultraviolet (visible) portions of the spectrum for 6% compressive (tensile) strain. Although its conduction band position is unfavorable for HER, its valence band edge is well-aligned to thermodynamically drive OER. The strong kinetic overpotential (1.51 eV for −6% compressive strain) for OER combined with low effective masses, makes it a promising candidate for integration in Z-scheme or heterojunction-based water splitting systems. Overall, Sr_3NF_3 emerges as a promising, stable and environmentally friendly photocatalyst for OER applications, with strain engineering offering a powerful pathway to optimize its performance.

Author contributions

Parmith Utsho: conceptualization, methodology, software, validation, writing – original draft, visualization. Manik Ibrahim: investigation, writing – review & editing, Md Sakib Hasan Khan: conceptualization, supervision, data curation, formal analysis, software, writing – review & editing. Md. Rafiqul Islam: resources, methodology, supervision, writing – review & editing.

Conflicts of interest

The authors declare that they have no known competing financial interests or personal relationships that could have appeared to influence the work reported in this article.

Data availability

The data that support the findings of this study are not publicly available at this time but will be made available from the corresponding authors. The raw computational data, including input files, optimized structures and calculated electronic and optical properties of Sr_3NF_3 under strain, are held by the authors and will be provided for research purposes subject to institutional approval and any applicable restrictions.

Supplementary information (SI) is available. See DOI: https://doi.org/10.1039/d5ra08652c.

Acknowledgements

The authors acknowledge the support from the computational facilities at Khulna University of Engineering & Technology.

References

1 D. S. A. A. Reza, K. Nazib, S. Afrin, Md. Islam and Md. H. A. Biswas, *Eng. Headway*, 2024, **5**, 13–24.
2 T. Jafari, E. Moharreri, A. S. Amin, R. Miao, W. Song and S. L. Suib, *Molecules*, 2016, **21**, 900.
3 *Global Hydrogen Review 2023*, https://www.iea.org/reports/global-hydrogen-review-2023, accessed October 2025.
4 H. Fu, Q. Zhang, Y. Liu, Z. Zheng, H. Cheng, B. Huang and P. Wang, *Angew. Chem., Int. Ed.*, 2024, **63**, e202411016.
5 R. Li, J. Luan, Y. Zhang, L. Jiang, H. Yan, Q. Chi and Z. Yan, *Renewable Sustainable Energy Rev.*, 2024, **206**, 114863.
6 H. Zhang, J. Liu, T. Xu, W. Ji and X. Zong, *Catalysts*, 2023, **13**, 728.
7 O. Khaselev and J. A. Turner, *Science*, 1998, **280**, 425–427.
8 S. Iqbal, B. Safdar, I. Hussain, K. Zhang and C. Chatzichristodoulou, *Adv. Energy Mater.*, 2023, **13**, 2203913.
9 A. Kudo and Y. Miseki, *Chem. Soc. Rev.*, 2009, **38**, 253–278.
10 F. Andrei, R. Zavoianu and I. C. Marcu, *Materials*, 2020, **13**, 5555.
11 M. Humayun, Z. Li, M. Israr, A. Khan, W. Luo, C. Wang and Z. Shao, *Chem. Rev.*, 2025, **125**, 3165–3241.
12 K. Maeda and K. Domen, *Bull. Chem. Soc. Jpn.*, 2016, **89**, 627–648.
13 M. Hojamberdiev, R. Vargas, F. Zhang, K. Teshima and M. Lerch, *Adv. Sci.*, 2023, **10**, 2305179.
14 K. Chen, J. Xiao, J. J. M. Vequizo, T. Hisatomi, Y. Ma, M. Nakabayashi, T. Takata, A. Yamakata, N. Shibata and K. Domen, *J. Am. Chem. Soc.*, 2023, **145**, 3839–3843.
15 K. Chen, J. Xiao, T. Hisatomi and K. Domen, *Chem. Sci.*, 2023, **14**, 9248–9257.
16 Z. Pan, T. Hisatomi, Q. Wang, S. Chen, M. Nakabayashi, N. Shibata, C. Pan, T. Takata, M. Katayama, T. Minegishi, A. Kudo and K. Domen, *ACS Catal.*, 2016, **6**, 7188–7196.
17 Y. Yao, Q. Li, W. Chu, Y. Ding, L. Yan, Y. Gao, A. Neogi, A. Govorov, L. Zhou and Z. Wang, *Phys. Chem. Chem. Phys.*, 2023, **25**, 32875–32882.
18 A. Miyoshi and K. Maeda, *Sol. RRL*, 2025, **5**, 2000521.
19 Q. Ain, J. Munir, H. Murtaza, A. S. Aldwayyan, H. M. Ghaithan, A. A. A. Ahmed and S. M. H. Qaid, *Cryst. Res. Technol.*, 2025, **60**, 2400184.
20 A. Fuertes, *APL Mater.*, 2020, **8**, 020903.
21 D. H. McTaggart, J. D. Sundberg, L. M. McRae and S. C. Warren, *Sci. Data*, 2023, **10**, 90.
22 C. Zhu, X. Niu, Y. Fu, N. Li, C. Hu, Y. Chen, X. He, G. Na, P. Liu, H. Zai, Y. Ge, Y. Lu, X. Ke, Y. Bai, S. Yang, P. Chen, Y. Li, M. Sui, L. Zhang, H. Zhou and Q. Chen, *Nat. Commun.*, 2019, **10**, 815.
23 B. Delley, *J. Chem. Phys.*, 1990, **92**, 508–517.
24 S. J. Clark, M. D. Segall, C. J. Pickard Ii, P. J. Hasnip, M. I. J. Probert, K. Refson and M. C. Payne, *Z. Kristallogr.*, 2005, **220**, 567–570.
25 K. Momma and F. Izumi, *J. Appl. Crystallogr.*, 2011, **44**, 1272–1276.
26 T. H. Fischer and J. Almlof, *J. Phys. Chem.*, 1992, **96**, 9768–9774.
27 J. Heyd, J. E. Peralta, G. E. Scuseria and R. L. Martin, *J. Chem. Phys.*, 2005, **123**, 174101.
28 J. Li, X. Wang, K. Liu, D. Li and L. Chen, *J. Superhard Mater.*, 2011, **33**, 173–178.
29 M. N. H. Liton, M. Roknuzzaman, M. A. Helal, M. Kamruzzaman, A. K. M. F. U. Islam, K. Ostrikov and M. K. R. Khan, *J. Alloys Compd.*, 2021, **867**, 159077.
30 G. Tang, X. Liu, S. Wang, T. Hu, C. Feng, C. Zhu, B. Zhu and J. Hong, *Mater. Horiz.*, 2024, **11**, 5320.
31 E. Mohebbi, E. Pavoni, D. Mencarelli, P. Stipa, E. Laudadio and L. Pierantoni, *Front. Mater.*, 2023, **10**, 1145822.
32 J. Bi, H. Lv, H. Wang, L. Du, Y. Liu, Y. Shen, B. Wu, Y. Wang and W. Ning, *Nanoscale*, 2025, **17**, 14263–14270.

33 X. Tang, W. Liu, C. Luo, X. Peng and J. Zhong, *RSC Adv.*, 2019, **9**, 12276–12281.
34 E. Mohebbi, E. Pavoni, C. Minnelli, R. Galeazzi, G. Mobbili, S. Sabbatini, P. Stipa, M. M. S. Fakhrabadi and E. Laudadio, *Nanomaterials*, 2024, **14**, 687.
35 Md. F. Rahman, Md. A. Rahman, R. Rahaman, M. S. H. Choudhury, Md. Z. Hasan, A. R. Chaudhry and A. Irfan, *Mater. Sci. Eng., B*, 2024, **308**, 117606.
36 G. Tang, P. Ghosez and J. Hong, *J. Phys. Chem. Lett.*, 2021, **12**, 4227–4239.
37 B. Yang, D. Bogachuk, J. Suo, L. Wagner, H. Kim, J. Lim, A. Hinsch, G. Boschloo, M. K. Nazeeruddin and A. Hagfeldt, *Chem. Soc. Rev.*, 2022, **51**, 7509–7530.
38 K. Maeda and K. Domen, *J. Phys. Chem. C*, 2007, **111**, 7851–7861.
39 G. Henkelman, A. Arnaldsson and H. Jónsson, *Comput. Mater. Sci.*, 2006, **36**, 354–360.
40 A. Kudo and Y. Miseki, *Chem. Soc. Rev.*, 2009, **38**, 253–278.
41 X. Chen, S. Shen, L. Guo and S. S. Mao, *Chem. Rev.*, 2010, **110**, 6503–6570.
42 O. Neufeld and M. C. Toroker, *J. Chem. Phys.*, 2016, **144**, 164704.
43 A. Walsh, J. Da Silva and S.-H. Wei, *Phys. Rev. B*, 2008, **78**, 075211.
44 H. Tang, K. Prasad, R. Sanjinès, P. E. Schmid and F. Lévy, *J. Appl. Phys.*, 1994, **75**, 2042–2047.
45 X. Liu and K. Sohlberg, *Comput. Mater. Sci.*, 2016, **123**, 1–7.
46 S. Barma, M. S. Hasan Khan, M. R. Islam and M. T. Hasan, *AIP Adv.*, 2023, **13**, 075020.
47 Y. Park, K. J. McDonald and K.-S. Choi, *Chem. Soc. Rev.*, 2013, **42**, 2321–2337.
48 Y. Sun, J. Lei, Y. Wang, Q. Tang and C. Kang, *RSC Adv.*, 2020, **10**, 17293–17301.
49 W. Zhang and Y. Chen, *J. Nanopart. Res.*, 2012, **15**, 1334.
50 S. Chen and L.-W. Wang, *Chem. Mater.*, 2012, **24**, 3659–3666.
51 S. Boukachabia, F. Z. Bentayeb and J. N. Gonçalves, *J. Electron. Mater.*, 1234, **52**, 5810–5821.
52 S. Franzen, *J. Phys. Chem. C*, 2008, **112**, 6027–6032.
53 A. K. Datta, M. K. Hossain, S. M. A. Haque, A. J. Sakib, N. Mia, M. Kaur, R. Sharma, L. Ben Farhat, A. M. Alsharari, N. Badi and V. K. Mishra, *Inorg. Chem. Commun.*, 2024, **170**, 113424.
54 G. Wang, A. Chernikov, M. M. Glazov, T. F. Heinz, X. Marie, T. Amand and B. Urbaszek, *Rev. Mod. Phys.*, 2018, **90**, 21001.
55 Z. Yang, A. Surrente, K. Galkowski, N. Bruyant, D. K. Maude, A. A. Haghighirad, H. J. Snaith, P. Plochocka and R. J. Nicholas, *J. Phys. Chem. Lett.*, 2017, **8**, 1851–1855.
56 T. Kirchartz and U. Rau, *Adv. Energy Mater.*, 2018, **8**, 1703385.
57 A. V. Gil Rebaza, A. Shankar and A. E. Aly, *Chem. Phys.*, 2025, **591**, 112565.
58 H. Pham, J. C. Neves, R. Yan, V. Pankratova, W. Cao and D. Zhang, *ACS Meas. Sci. Au*, 2025, **5**, 666–676.
59 Md. S. Hasan Khan, Md. R. Islam and Md. T. Hasan, *AIP Adv.*, 2020, **10**, 085128.
60 G. M. Khatamunnaby, M. S. Hasan Khan, M. T. Hasan, M. R. Islam and M. Z. Rahman, *AIP Adv.*, 2024, **14**, 025147.
61 Md. F. Rahman, Md. A. I. Islam, Md. R. Islam, Md. H. Ali, P. Barman, Md. A. Rahman, Md. Harun-Or-Rashid, M. Hasan and M. K. Hossain, *Nano Select*, 2023, **4**, 632–645.
62 A. Ghosh, M. F. Rahman, M. R. Islam, M. S. Islam, M. Amami, M. K. Hossain and A. B. Md Ismail, *Heliyon*, 2023, **9**, e19271.
63 M. S. Daw and M. I. Baskes, *Phys. Rev. Lett.*, 1983, **50**, 1285–1288.
64 S. Shakeel, P. Song, S. H. Shah, Z. Zada, T. Huang, A. Laref, N. Hakimi and M. Faizan, *Mater. Chem. Phys.*, 2024, **324**, 129683.
65 A. Mera, M. A. Rehman and Z. ur Rehman, *Chin. J. Phys.*, 2024, **87**, 268–283.
66 M. Harun-Or-Rashid, M. Ferdous Rahman, M. Monirul Islam, M. K. A. Mohammed and M. Z. Bani-Fwaz, *Inorg. Chem. Commun.*, 2024, **168**, 112864.
67 X. Chen and S. S. Mao, *Chem. Rev.*, 2007, **107**, 2891–2959.
68 S. Belhachi, S. Al-Qaisi, S. Samah, H. Rached, A. Zaman, T. A. Alrebdi, A. Boutramine, N. Erum, R. Ahmed and A. S. Verma, *J. Inorg. Organomet. Polym. Mater.*, 2025, **35**, 978–993.
69 A. K. Datta, M. K. Hossain, S. M. A. Haque, A. J. Sakib, N. Mia, M. Kaur, R. Sharma, L. Ben Farhat, A. M. Alsharari, N. Badi and V. K. Mishra, *Inorg. Chem. Commun.*, 2024, **170**, 113424.
70 S. K. Yadav, S. Dahal, R. Khadka, B. Guragain, P. Pokharel, P. Oli and D. Adhikari, *Eng. Rep.*, 2025, **7**, e13115.